Chem. Senses 40: 73–87, 2015
doi:10.1093/chemse/bju061
Advance Access publication December 12, 2014

Co-expression of Anoctamins in Cilia of Olfactory Sensory Neurons

Bastian Henkel[1,2,3], Daniela R. Drose[4], Tobias Ackels[4], Sonja Oberland[1,2,3], Marc Spehr[4] and Eva M. Neuhaus[1,2]

[1]Department of Pharmacology and Toxicology, University Hospital Jena, Drackendorfer Strasse 1, 07747 Jena, Germany, [2]Cluster of Excellence NeuroCure, Charité-Universitätsmedizin Berlin, Charitéplatz 1, 10117 Berlin, Germany, [3]FU Berlin, Fachbereich Biologie, Chemie und Pharmazie, Takustr. 3, 14195 Berlin, Germany and [4]Department of Chemosensation, Institute for Biology II, RWTH Aachen University, Worringerweg 3, 52074 Aachen, Germany

Correspondence to be sent to: Eva M. Neuhaus, Department of Pharmacology and Toxicology, University Hospital Jena, Drakendorfer Street 1, 07747 Jena, Germany. e-mail: eva.neuhaus@med.uni-jena.de

Accepted November 13, 2014

Abstract

Vertebrates can sense and identify a vast array of chemical cues. The molecular machinery involved in chemodetection and transduction is expressed within the cilia of olfactory sensory neurons. Currently, there is only limited information available on the distribution and density of individual signaling components within the ciliary compartment. Using super-resolution microscopy, we show here that cyclic-nucleotide-gated channels and calcium-activated chloride channels of the anoctamin family are localized to discrete microdomains in the ciliary membrane. In addition to ANO2, a second anoctamin, ANO6, also localizes to ciliary microdomains. This observation, together with the fact that ANO6 and ANO2 co-localize, indicates a role for ANO6 in olfactory signaling. We show that both ANO2 and ANO6 can form heteromultimers and that this heteromerization alters the recombinant channels' physiological properties. Thus, we provide evidence for interaction of ANO2 and ANO6 in olfactory cilia, with possible physiological relevance for olfactory signaling.

Key words: anoctamin, cilia, CNG, olfactory, STED

Introduction

In the main olfactory epithelium, canonical olfactory transduction mechanisms are well understood (Munger et al. 2009; Pifferi et al. 2010). Odorant receptors on cilia of olfactory sensory neurons (OSNs) bind odorous molecules (Buck and Axel 1991; Kato and Touhara 2009) and activate adenylyl cyclase type III (ACIII) (Wong et al. 2000) *via* $G\alpha_{olf}$ (Belluscio et al. 1998). The resulting rise in cAMP opens cyclic-nucleotide-gated (CNG) non-selective cation channels leading to influx of Ca^{2+} and Na^{+} (Nakamura and Gold 1987; Pifferi et al. 2006). Increased cytosolic Ca^{2+} opens Ca^{2+}-activated Cl^{-} channels in the ciliary membrane (Kleene and Gesteland 1991; Reisert et al. 2003), substantially amplifying the primary CNG channel current (Lowe and Gold 1993; Reisert et al. 2005). This chloride current is responsible for up to 90% of the receptor current (Kurahashi and Yau 1993; Reisert et al. 2005; Boccaccio and Menini 2007). ANO2, a member of the recently identified anoctamin family of Ca^{2+}-activated Cl^{-} channels (Caputo et al. 2008; Schroeder et al. 2008; Yang et al. 2008), is specifically expressed in cilia of mature OSNs (Stephan et al. 2009; Hengl et al. 2010; Rasche et al. 2010; Dauner et al. 2012). Although the functional significance of ANO2-mediated chloride currents in mouse olfaction remains somewhat controversial (Billig et al. 2011), ANO2 clearly forms a chloride channel in OSN cilia (Stephan et al. 2009; Sagheddu et al. 2010).

A critical aspect of cellular signaling is the spatial arrangement of the interacting molecular components. The OSN response to individual odorant-binding events is spatially restricted (Bhandawat et al. 2005). In case of only few unitary events, the associated transduction domains are spatially segregated and do not interact, therefore summing linearly (Bhandawat et al. 2005 2010). Moreover, recordings of Ca^{2+} changes in individual cilia provide evidence for Ca^{2+} microdomains (Castillo et al. 2010). The shape, duration, and kinetics of individual events resembles single CNG channel fluctuations, indicating that microdomains typically contain 1 to 3 CNG channels (Castillo et al. 2010). How the different signaling molecules are spatially organized in order to

ensure the speed and specificity of signaling remains poorly understood. PDZ (postsynaptic density protein [PSD95], Drosophila disc large tumor suppressor [Dlg1], and zonula occludens-1 protein [zo-1]) scaffolding proteins assemble macromolecular "transducisomes" in mouse OSNs (Dooley et al. 2009; Baumgart et al. 2014) and contribute to the organization of signaling microdomains.

Localization and spatial arrangement of olfactory signaling proteins along the thin ciliary compartment cannot be analyzed by conventional diffraction-limited optical methods. In this study, we use 2-color stimulated emission depletion (STED) microscopy to investigate the formation of spatially discernible membrane microdomains as putative signaling platforms. By analyzing the distribution of olfactory transduction channels, we show that CNG channels and anoctamins localize to discrete foci in olfactory cilia. Thus, we provide optical evidence for a distinct spatial organization of ion channels in OSN cilia. Furthermore, we show that, in addition to ANO2, ANO6 is localized in olfactory cilia microdomains, likely *via* direct interaction with ANO2. As heterologous co-expression of both channels results in supra-additive chloride currents, this interaction could shape the physiological OSN response profile *in vivo*.

Materials and methods

Animals

All animal procedures were in compliance with the European Union legislation (Directive 86/609/EEC) and FELASA (Federation of Laboratory Animal Science Associations) recommendations. C57BL/6 mice (Charles River Laboratories) were housed at room temperature in a 12:12-h light:dark cycle with food and water *ad libitum*. The study was approved by the Lageso (Landesamtes für Gesundheit und Soziales Berlin).

Antibodies

Following primary antibodies were used: anti-acetylated tubulin mouse monoclonal (T-6793, Sigma); anti-CNGA2 goat polyclonal (sc-13700, Santa Cruz); anti-CNGA2 rabbit polyclonal (APC-045, Alomone Labs); anti-CNGA4 rabbit polyclonal (Michalakis et al. 2006); anti-ANO2 rabbit polyclonal (Rasche et al. 2010); anti-ANO6 rat polyclonal (Martins et al. 2011); anti-GFP mouse monoclonal (11814460001, Roche); and anti-*Renilla* luciferase mouse monoclonal (MAB4400, Millipore). The anoctamin antibodies were used for immunohistochemical stainings and western blotting experiments. Following secondary antibodies were used: donkey-anti-mouse Alexa 488 (Invitrogen); donkey-anti-goat Alexa 488 (Invitrogen); goat-anti-rabbit Oregon Green 488 (Invitrogen); V500 Streptavidin (561419, BD); donkey-anti-goat biotin (AP180B, Millipore); donkey-anti-rabbit biotin (711-065-152, Jackson); donkey-anti-mouse biotin (715-065-150, Jackson); goat-anti-rabbit horseradish peroxidase (Biorad); goat-anti-mouse horseradish peroxidase (Biorad); goat-anti-rabbit Abberior 440 SX (Abberior); and goat-anti-mouse Oregon Green 514 (Invitrogen).

Immunohistochemical staining

Adult mice were sacrificed. After removal of the nasal bones (*os nasale*), the skinned head was incubated in 4% paraformaldehyde (PFA) at 4 °C for 2 h and subsequently in 30% sucrose (in Ringer's solution) overnight, embedded in tissue freezing medium (Leica Biosystems), and stored at −80 °C. Cryosections (10 µm) of the main olfactory epithelium were blocked (phosphate-buffered saline [PBS] + 1% gelatin, 0,1% Triton-X100) for 1 h at room temperature, incubated with antibodies, and mounted in Prolong Antifade Gold reagent (Life Technologies). For 2-color staining, sections were incubated with diluted primary antibodies at 4 °C overnight. On the next day, sections were washed 3× with PBS buffer for 5 min and incubated with diluted biotin-coupled secondary antibodies for 2 h at room temperature, followed by Streptavidin-coupled V500 and Oregon Green 488-coupled secondary antibodies for 2 h at room temperature. For anoctamin costaining, cryosections were incubated first with anti-ANO6 antibody overnight, followed by Oregon Green 488-coupled secondary antibodies and blocking of remaining rabbit epitopes by incubation with anti-rabbit FAB fragments for 2 h at room temperature. FAB fragments were post-fixed with 4% PFA solution for 5 min. The sections were incubated with anti-ANO2 antibody overnight, stained with biotin-coupled secondary antibody and streptavidin-coupled V500.

Two-color STED—image acquisition

We used a single-depletion laser method for 2-color STED microscopy that permits the use of commercial fluorescent labels (Schmidt et al. 2008). We evaluated the characteristics of several fluorophores that have a high cross-section for stimulated emission at the depletion wavelength of 592 nm, and that can be excited with the argon laser lines at 458 (V500 and Abberior STAR 440SX) or 514 nm (Alexa 488, Oregon 488, and Oregon 514). V500 and Oregon Green 488 showed the most robust signal in the desired channel without cross-talk and were used for all experiments. Images were taken with a Leica SP5 II laser confocal scan head (Leica Microsystems) based on a Leica DMI6000 inverse microscope (Leica Microsystems) equipped with an argon laser (458–514 nm), a STED CW depletion laser (592 nm), and 2 Leica HyD detectors. To minimize cross-excitation, we switched excitation lasers between line scans. V500 and Oregon Green 488 emission were detected at 465–500 and 540–585 nm, respectively. To ensure that neither cross-talk nor bleed-through between channels occurs, double staining was accompanied by experiments in which 1 primary

antibody was omitted. After STED image acquisition, LAS AF software was used to calculate a point spread function and subsequently deconvolute the STED image using the LAS AF STED/confocal deconvolution algorithm. In the confocal mode, the full width at half maximum of the fluorescent spots was 250 nm and in STED mode, the full width at half maximum was 75 nm. In order to visualize resolution improvement, a confocal image was gathered before every STED image recording with the same image settings.

Cloning of expression vectors

GFP^2 and *Renilla* luciferase genes were amplified by polymerase chain reaction from GFP^2-*R*Luc(h) positive control vector (6310030, Perkin Elmer) and cloned into pcDNA3.1 (Invitrogen). *ANO2* and *ANO6* genes were amplified from mouse olfactory epithelium cDNA and cloned as N- or C-terminal fusion constructs with GFP^2 and *Renilla* luciferase (ANO6, NP_780553.2 ANO2, XP_006506182.1; Stephan et al. 2009). Control constructs of untagged anoctamin genes were generated by cloning into pcDNA3.1. The construct encoding the tetracysteine motif (ANO2-TC) was cloned into pcDNA3.1 by adding the tag to the reverse primer sequence (Giepmans et al. 2006).

GFP_fwd GCAAGCTTACCATGGAATTCGTGAGCA AGG GCGAGGAGCTGTTCACC
GFP_rev GCCTCGAGTTAAGCGGCCGCCTTGTA CA GCTCGTCCATGC
Luc_fwd GCAAGCTTACCATGGAATTCACCAGCAA GGTGTACGACC
Luc_rev GCCTCGAGTTAAGCGGCCGCCTGCTC GTTCTTCA GCACTCTCTCC
Ano1-Cterm_fwd GCAAGCTTACCATGAGG GTCCCCGAGAAGTACTCG
Ano1-Cterm_rev GCGAATTCCCAGCGCGTC CCCATGGTACTCG
Ano2-Cterm_fwd GCGAATTCCACTTTCACGACAAC CAGAGGAAAGTC
Ano2-Cterm_rev GCGAATTCTACATTGGTGT GCTGGGAC
Ano2-Nterm_fwd TTGCGGCCGCTCACTTTCA CGACA ACCAGAGGA AAGTC
Ano2-Nterm_rev TTAGCGGCCGCTACATTGGTGTG CTGGGAC
Ano2-TC_fwd ATTGAATTCCCACCATGGCGGCCCC TGGGCT
Ano2-TC_rev ATTGCGGCCGCTCATTACTACGG TTCCATGCA GCAGCCCGGGC AGCAGTTCAGAAATACATTGGTGTGCTGGGAC CCT
Ano6-Cterm_fwd GCGAATTCCAGATGATGACTAG GAAGGTCC
Ano6-Cterm_rev GCGAATTCTTCGAGTTTTG GCCGC
Ano6-Nterm_fwd TTGCGGCCGCTCAGATGATGAC TAGGAAGGTCC
Ano6-Nterm_rev TTAGCGGCCGCTTCGAGT TTTGGCCGC

Western blotting

Human embryonic kidney 293 (HEK293) cells were seeded and grown to 90% confluence for 2 days in DMEM GlutaMax (Life Technologies) supplemented with penicillin/streptomycin (PAA), and transfected with turbofect (Thermo Scientific) according to the manufacturer's instructions. After 24 h of protein expression, cells were lysed in ice-cold buffer (5 mM Tris–HCl, 300 mM sucrose, 0.1 mM EDTA + protease inhibitor cocktail [Roche]), cell debris was removed *via* centrifugation (1500× *g*, 15 min), and the supernatant was centrifuged for 35 min at 20 000× *g* for membrane protein preparation. The membrane pellet was resuspended in PBS buffer containing 1% CHAPSO (C3649, Sigma) and the same amount of proteins were diluted in 10 µL of sodium dodecyl sulfate (SDS) loading buffer (0.02% [w/v] bromophenol blue, 20% [v/v] glycerol, 4% [w/v] SDS, 200 mM dithiothreitol, 125 mM Tris), separated by SDS gel electrophoresis, and blotted to nitrocellulose membrane (10401196, GE Healthcare). Proteins were detected *via* specific antibodies using the electrochemiluminescence detection system.

Bioluminescence resonance energy transfer assay

For bioluminescence resonance energy transfer (BRET) assays, approximately 12 000 HEK293 cells per well were grown in white 96-well plates (Thermo Scientific) for 2 days. Cells were transfected with anoctamin *Renilla* luciferase or GFP fusion constructs and probed for BRET activity after 24 h. Each well was transfected with 200 ng of plasmid using 0.4 µL of turbofect reagent. Plasmid and turbofect concentrations were raised accordingly for double transfection and varying donor:acceptor ratios. 200-ng donor plasmid + 200-ng acceptor plasmid with 0.8 µL of turbofect for ratio 1:1, 200-ng donor plasmid + 300-ng acceptor plasmid with 1.0 µL of turbofect for ratio 1:1.5, 200-ng donor plasmid + 400-ng acceptor plasmid with 1.2 µL of turbofect for ratio 1:2. Cells were incubated in 30 µL of PBS containing 7.5 µM of coelenterazine 400a (Santa Cruz) and 0.1% Pluronic F-127 (Life Technologies). Bioluminescence and fluorescence signals were detected immediately with a Mitras LB940 plate reader (Berthold) using the Berthold BRET^2 emission filter pack.

All BRET experiments were performed while the cells remained attached to the 96-well plates. The values were corrected by subtracting the background BRET signal detected when the *R*Luc construct was expressed alone. The BRET signal is the ratio between GFP (acceptor) fluorescence and luciferase (donor) bioluminescence, and was calculated for different combinations of anoctamins. Every BRET signal represents the arithmetic mean of 5 technical replicates.

Specificity of the measured signals was determined by monitoring BRET values for raising acceptor versus donor ratios. Corresponding untagged anoctamin constructs were used as negative controls instead of GFP-tagged anoctamins. Numbers of experiments (*n*) are stated in diagrams. All data are presented as arithmetic mean ± standard error of the mean (SEM). BRET values of GFP-tagged anoctamins were compared with untagged negative controls by Student's *t*-test to test for statistically significant differences between the measured BRET signals (*$P < 0.05$, **$P < 0.01$, ***$P < 0.001$).

Chemicals for electrophysiological recordings and ratiometric fura-2 imaging

a) Extracellular solution (S_1) containing (in mM): 145 NaCl, 5 KCl, 1 $CaCl_2$, 1 $MgCl_2$, 10 HEPES; pH = 7.3 (adjusted with NaOH); osmolarity = 300 mOsm (adjusted with glucose). b) Extracellular TEA solution (S_2) containing (in mM): 124 NaCl, 15 TEACl, 1 $MgCl_2$, 1 $CaCl_2$, 10 HEPES; pH = 7.3; osmolarity = 300 mOsm. c) Reduced chloride solution (S_3) containing (in mM): 119 Na gluconate, 15 TEACl, 1 Ca gluconate, 1 Mg gluconate, 5 CsCl, 10 HEPES; pH = 7.3 (NaOH); osmolarity = 300 mOsm. d) Ca^{2+}-free extracellular solution (S_4) containing (in mM): 110 NaCl, 40 NaOH, 5 KCl, 1 $MgCl_2$, 10 EGTA, 10 HEPES; pH = 7.3 (NaOH); osmolarity = 300 mOsm. e) High Ca^{2+} extracellular solution (S_5) containing (in mM): 125 NaCl, 5 KCl, 10 $CaCl_2$, 1 $MgCl_2$, 10 HEPES; pH = 7.3 (NaOH); osmolarity = 300 mOsm. f) Pipette solution (S_6) containing (in mM): 138 CsCl, 2 CsOH, 1 EGTA, 10 HEPES, 1 MgATP, 0.5 NaGTP, 0.3 $CaCl_2$; pH = 7.1 (CsOH); osmolarity = 290 mOsm. Free Ca^{2+} concentration (S_6: 110 nM) was calculated using WEBMAXC STANDARD. If not stated otherwise, chemicals were purchased from Sigma. Final dimethyl sulfoxide concentrations were less than or equal to 0.1%. Solutions and pharmacological agents were applied *via* an 8-in-1 multibarrel "perfusion pencil" (Veitinger et al. 2011a).

HEK293T cells were cultured in DMEM (100 U/mL penicillin; 100 µg/mL streptomycin) supplemented with 10% fetal calf serum as previously described (Veitinger et al. 2011b). Transfection of semiconfluent HEK293T cells with full-length polymerase chain reaction products cloned into pcDNA3 vectors (Invitrogen) was conducted using Mirus TransIT-LT1 and transfection efficiency was monitored as described (Veitinger et al. 2011b). Ca^{2+} imaging and electrophysiological experiments were performed 24–48 h after transfection.

Ca^{2+} imaging

HEK293T cells, grown on 35 mm glass-bottom dishes, were loaded with fura-2/AM (3 µM; 30 min; 25 °C; S_1). Dye-loaded cells were washed in S_1 and transferred to the stage of an inverted microscope (Leica DMI4000B, Leica Microsystems) equipped for ratiometric live-cell imaging with a Visichrome polychromator system (Visitron Systems) for multiwavelength excitation, a 12-bit 1392 × 1040 pixel monochrome CCD camera (CoolSnap EZ, Photometrics), and LAS MMAF imaging software (Leica Microsystems). About 10–30 cells in randomly selected fields of view were viewed at 200× magnification and illuminated sequentially at 340 and 380 nm (cycle time 1000 ms). The average pixel intensity within user-selected regions of interest was digitized and stored. Ca^{2+}-dependent fluorescence signals at 510 nm were calculated as the f_{340}/f_{380} intensity ratio. In experiments designed to calculate Ca^{2+} concentrations $[Ca^{2+}]$ rather than relative changes, integrated fluorescence signals from individual regions of interests were background subtracted and $[Ca^{2+}]$ was calculated according to Grynkiewicz et al. (1985) using the equation $[Ca^{2+}] = K_d * (F_0/F_s) * [(R - R_{min})/(R_{max} - R)]$, where R is the experimentally derived fluorescence intensity ratio (f_{340}/f_{380}), R_{min} and R_{max} are ratios measured using $[Ca^{2+}]_{zero}$ and saturating Ca^{2+} calibration solutions (S_4 and S_5), respectively, K_d is the fura-2 dissociation constant (224 nM), and F_0 and F_s are proportionality coefficients for free and Ca^{2+}-bound fura-2, respectively (measured at 380 nm excitation). R_{min} and R_{max} were determined in intact cells by applying 5 µM of ionomycin in $[Ca^{2+}]_{zero}$ (10 mM of EGTA) and saturating Ca^{2+} (10 mM of Ca^{2+}). Values for R_{min}, R_{max}, and F_0/F_s were 0.56, 0.85, and 1.88, respectively.

Electrophysiology

For electrophysiological recordings, HEK293T cells were transferred to the stage of an inverse video-microscope (DMI4000B, Leica Microsystems). Cells were continuously superfused with solution S_1 (~3 mL/min; gravity flow) at room temperature. Patch pipettes with a resistance of approximately 5 MΩ were pulled from borosilicate glass capillaries with filament and fire-polished ends (1.50 mm OD/0.86 mm ID; Science Products) on a PC-10 vertical 2-step micropipette puller (Narishige Instruments) and fire-polished using a MF-830 microforge (Narishige Instruments). Recording pipettes were filled with S_6 solution. An EPC-10 amplifier controlled by Patchmaster 2.67 software (HEKA Elektronik) was used for data acquisition. Both pipette (C_{fast}) and cell membrane capacitance (C_{slow}) were monitored and automatically compensated throughout the experiment. Measured C_{slow} values served as an approximation of the cell surface area for normalization of current amplitudes (i.e., current density). HEK293T cells with unstable C_{slow} values and R_{series} > 30 MΩ were not considered for further analysis. Theoretical liquid junction potentials were calculated using JPCalcW software and automatically corrected online. Signals were low-pass filtered (2.5 kHz; analog 3- and 4-pole Bessel filters in series) with a sampling rate of 10 kHz. Electric noise was suppressed using a Hum Bug Noise Eliminator (Quest Scientific). Between recordings, cells were kept at a holding

potential (V_{hold}) of −60 mV. Experiments were performed using ramp protocols (−100 to +100 mV; 500-ms duration) with up to 150 repetitions. Continuous recordings were performed at V_{hold} = −80 mV.

Average current densities at 80 mV and +80 mV were determined by averaging recorded values sampled during a time/voltage "window" of 2.5 ms/1 mV, respectively (250 data points).

All data were obtained from experiments performed on at least 2 days. Individual numbers of cells/experiments (n) are denoted in figure legends. For ramp protocol analysis, 5 ramps before stimulation were averaged and subtracted from the peak amplitude ramp recorded during stimulation (maximum currents developed 5–6 s after stimulus onset; 5.0 ± 0.4 s [ANO2]; 5.8 ± 0.4 s [ANO6]; 6.3 ± 0.4 s [ANO2/ANO6]). If not stated otherwise, results are presented as mean ± SEM, and statistical analyses were performed using paired or unpaired t-tests (as dictated by experimental design). Dose–response curves were calculated based on averaged ATP-induced currents recorded at constant V_{hold} and averaged Ca^{2+} concentration changes observed in response to ATP under the same experimental conditions. Ca^{2+} imaging and electrophysiological data were analyzed offline using Patchmaster 2.67 (HEKA Elektronik), IGOR Pro 6.31 (WaveMetrics), and Excel (Microsoft) software. Dose–response curves were fitted by the Hill equation.

Results

Anoctamin expression in the olfactory system

ANO2 is a major constituent of the calcium-activated chloride channel in olfactory cilia (Stephan et al. 2009; Billig et al. 2011), but the presence and potential role of other anoctamin isoforms in OSN cilia is unclear. Besides ANO2, we have previously identified ANO1 and ANO6 in the mouse olfactory epithelium by proteomic methods (Rasche et al. 2010). We therefore stained olfactory epithelium cryosections with antibodies against ANO1, ANO2, and ANO6 together with acetylated tubulin as a cilia marker (Figure 1). Confocal microscopy confirmed that ANO2 is present in olfactory cilia, whereas ANO1 is absent, supporting previous findings (Billig et al. 2011). In addition, we found ANO6 co-localized to acetylated tubulin in the olfactory signaling compartment. Specificity of the ANO6 antibody (Martins et al. 2011) was controlled in both heterologous cells and the olfactory epithelium (Supplementary Figure S1).

Olfactory signaling proteins are organized in segregated microdomains

In high-magnification confocal images, we noticed a non-homogenous distribution of anoctamin proteins in the ciliary layer. To investigate the spatial organization of ciliary channels, we employed STED microscopy, an optical technique that breaks the resolution limit of light microscopy (Dyba et al. 2003). Conventional confocal images of OSN cilia stained for ANO2 showed blurred staining (Figure 2A). Using STED microscopy, the ANO2 staining appeared as discrete spots (Figure 2A).

For high-resolution analysis of channel localization, we established STED microscopy for 2-color staining of mouse olfactory epithelium cryosections (Supplementary methods and Supplementary Figures S2 and S3). We then analyzed expression patterns of the A2 subunit of the olfactory CNG channel labeled together with acetylated tubulin as ciliary marker (Figure 2B). High-magnification STED images showed CNGA2 localization in discrete spot-like structures, in contrast to a more homogeneous appearance of the tubulin staining (Figure 2B). Using STED microscopy, ANO2 staining also transformed into discrete spots co-localized to cilia, which were stained with antibodies against acetylated tubulin (Figure 2C). In confocal images, ANO6 and ANO2 localization was comparable (Figure 1). Similar to ANO2, the ANO6 staining appeared as distinct foci when using STED microscopy (Figure 2D). Because cilia density in the olfactory epithelium is very high and because we investigate proteins that are abundantly expressed in most, if not all, OSN cilia, it is impossible to follow the distribution of channels along an entire individual cilium. Such analysis is possible in isolated OSNs (Supplementary Figure S4). However, we observed substantial redistribution of signaling proteins upon dissociation (Supplementary Figure S4), rendering detailed ciliary protein localization studies in isolated OSNs difficult to interpret. Together, STED microscopy revealed distinct foci of antibody labeled ion channels in olfactory cilia.

Being able to resolve single spots of olfactory signaling proteins (Figure 2), we quantified ANO2, ANO6, and CNGA2 foci in defined areas of olfactory cilia (marked by tubulin staining). Compared with conventional confocal imaging, low-magnification STED microscopy showed a relatively homogenous distribution and density of the labeled spots (Figure 3A–C). For further analysis, we defined a protein "patch" as a spatially segregated accumulation of fluorescence, and we quantified patch diameter and density for all 3 channel proteins. Although the density of CNGA2- and ANO6-positive patches did not significantly differ (2.88 ± 0.07/μm^2 and 2.71 ± 0.09/μm^2, respectively), ANO2 patch density was significantly higher (4.99 ± 0.12/μm^2). However, patch diameters were similar (ANO2 127 ± 3 nm, ANO6 132 ± 2 nm, CNGA2 111 ± 2 nm; Figure 3E). Together, STED microscopy provided morphological evidence for the organization of anoctamins and CNG channels in distinct domains, indicating the existence of signaling microdomains in olfactory cilia.

Both ANO2 and ANO6 are Ca^{2+}-activated chloride channels

The function of ANO6 as a Ca^{2+}-dependent chloride channel is controversial (Kunzelmann et al. 2014). We therefore

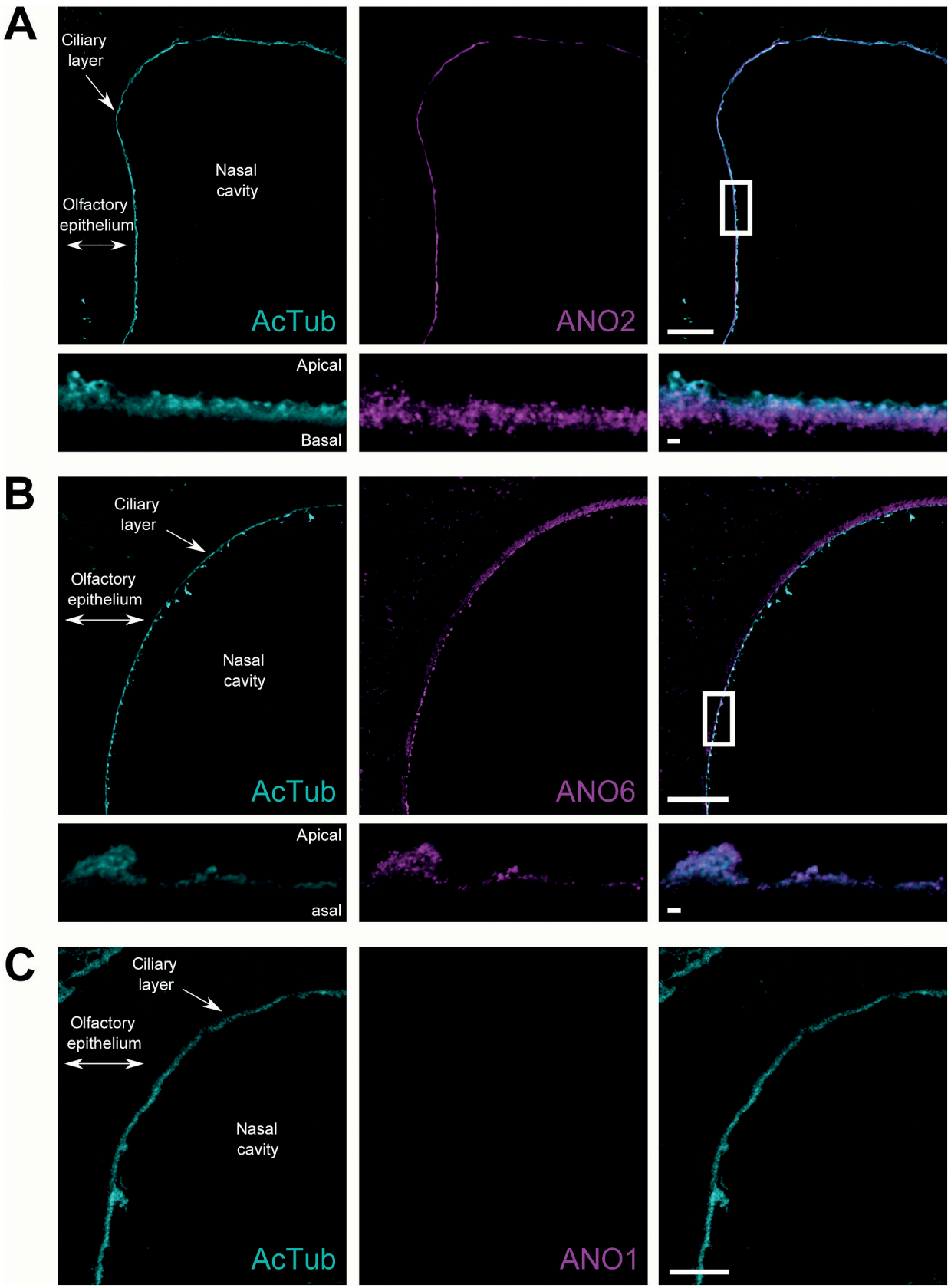

Figure 1 ANO2 and ANO6 are expressed in olfactory cilia. Cryosections of olfactory epithelium were stained for different anoctamins. (**A**) ANO2, (**B**) ANO6, and (**C**) ANO1. Anoctamin stainings are shown in magenta, acetylated tubulin (cyan) was used to label the ciliary layer, scale bars = 75 μm. Boxed regions were magnified to show the ciliary layer in greater detail, scale bars = 1 μm.

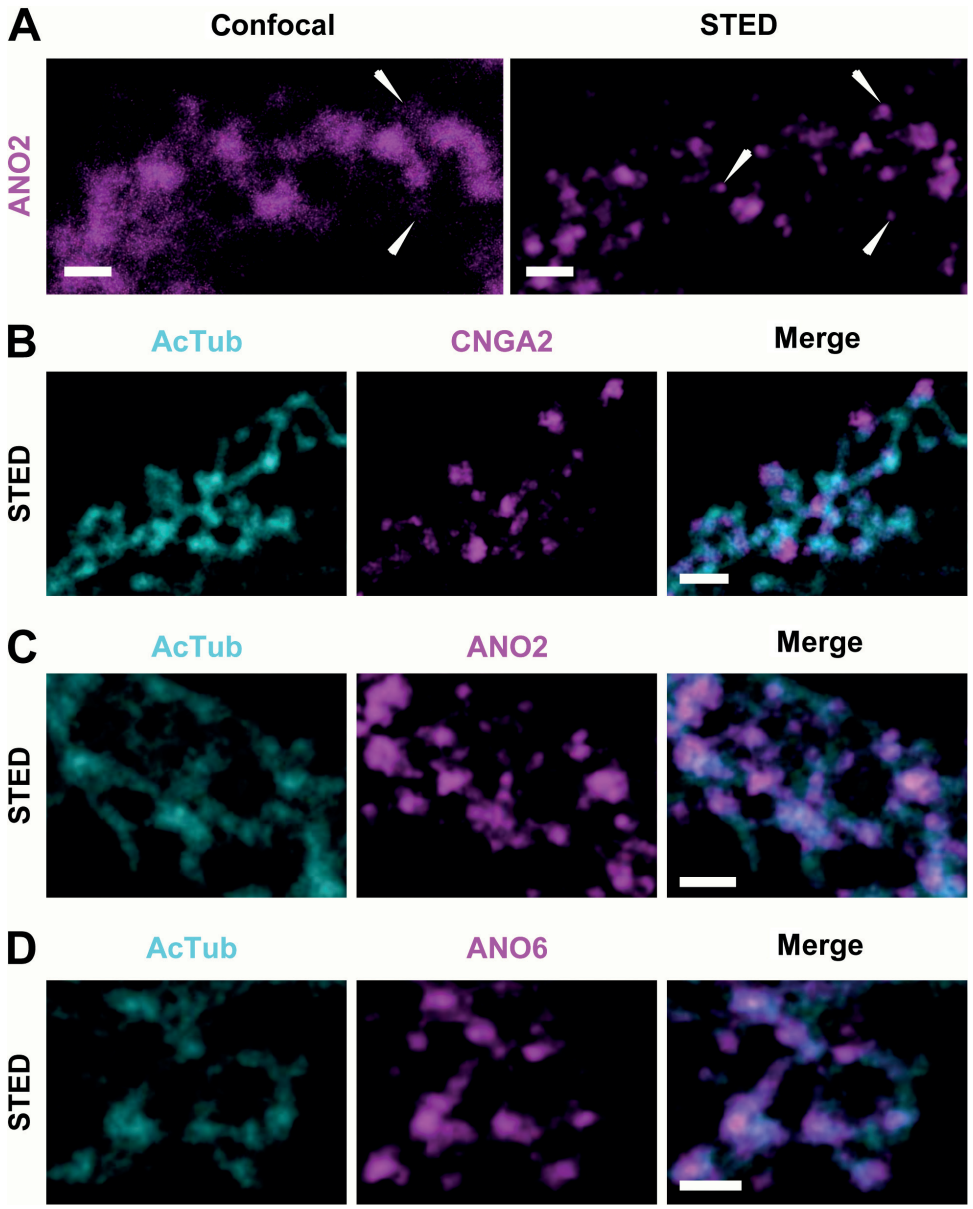

Figure 2 Clustered localization of CNGA2 and anoctamins in olfactory cilia. (**A**) Frontal sections of olfactory epithelium were stained for ANO2 and analyzed with conventional confocal and STED microscopy, demonstrating the increase in resolution when switching to the STED mode. Single clusters that were not visible in the confocal picture (examples are indicated by arrowheads) can clearly be seen in STED pictures. Co-localization of (**B**) CNGA2, (**C**) ANO2 and (**D**) ANO6 (magenta) and acetylated tubulin (cyan), showing clusters stained by the different antibodies. Scale bars = 500 nm.

analyzed the electrophysiological properties of recombinant ANO2 and ANO6 in HEK293T cells (Figure 4). Cells were stimulated with ATP to trigger Ca^{2+} release from internal stores (Veitinger et al. 2011b), thereby activating overexpressed anoctamins (Yang et al. 2008). In whole-cell voltage-clamp recordings at constant holding potential (V_{hold} = −80 mV), we observed robust negative currents in ANO2-expressing cells (Figure 4B, inset) in response to different ATP concentrations (10 and 100 µM). To characterize these currents, we performed voltage ramp recordings (−100 to +100 mV; 500-ms duration) using different extracellular solutions (S_2, S_3, S_2 + niflumic acid). Replacement of extracellular chloride with gluconate induced a reversal potential shift to more positive values (Figure 4B). Moreover, currents were abolished by niflumic acid, a well-described chloride channel blocker (Figure 4B). These results confirm that ANO2 acts as a Ca^{2+}-activated Cl^- channel (Schroeder et al. 2008; Pifferi et al. 2009; Stephan et al. 2009). Under identical conditions, non-transfected HEK293T cells did not show ATP-induced currents (Supplementary Figure S5). For quantification, we calculated average current densities at −80 and +80 mV (Figure 4C). Under symmetric chloride conditions (solution S_2), current densities were −4.36 ± 1.7 pA/pF and 8.67 ± 1.9 pA/pF, respectively (n = 14; 10 µM of

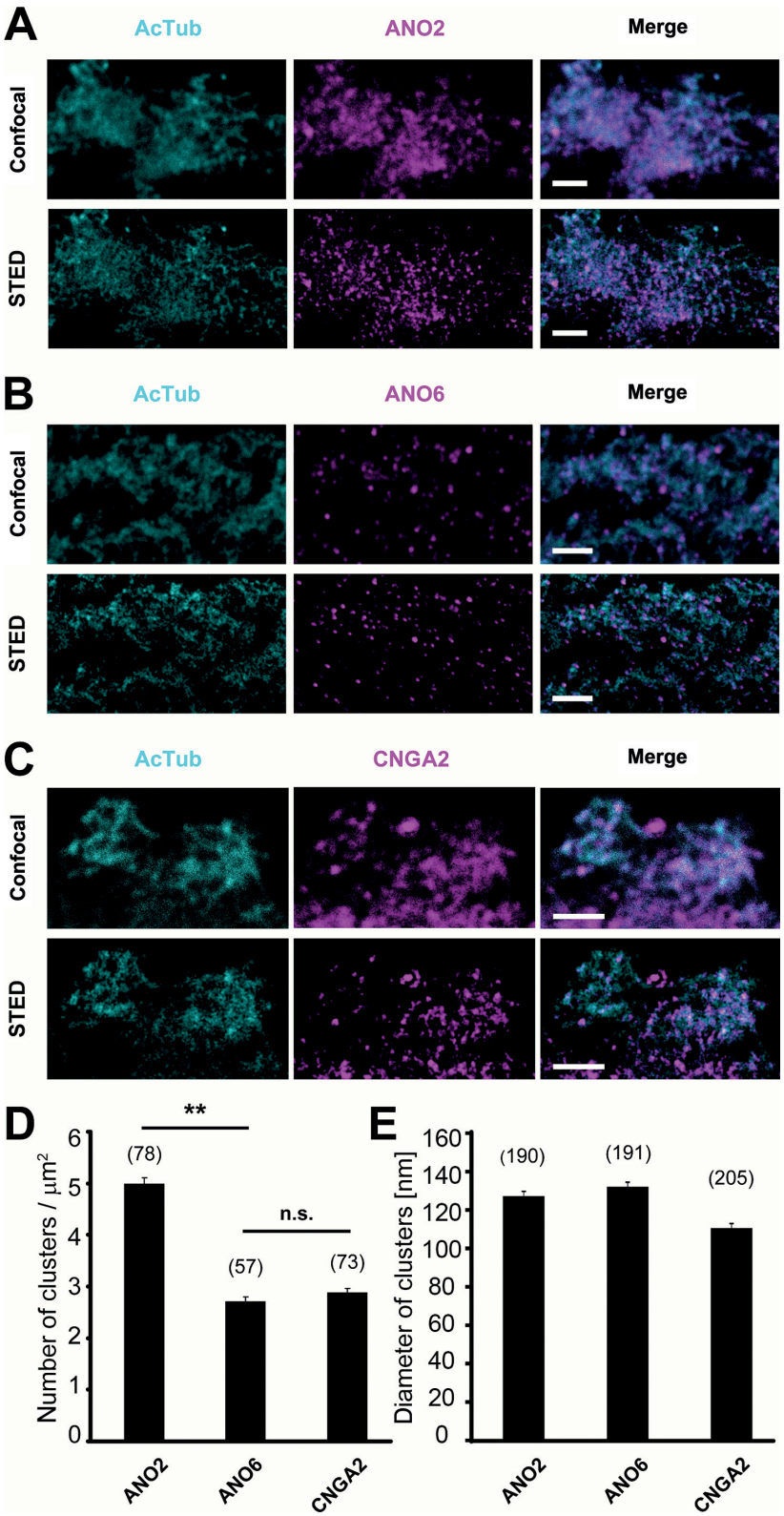

Figure 3 Analysis of ion channel clusters in olfactory cilia. Frontal sections of olfactory epithelium were stained for ANO2, ANO6 and CNGA2 (magenta), and acetylated tubulin (cyan). (**A–C**) Confocal and STED images of larger areas of olfactory cilia (compare with Figure 2) stained for ANO2 (A), ANO6 (B) and CNGA2 (C). Scale bars = 1 µm. (**D**) Number of ANO2, ANO6, and CNGA2 clusters co-localized to acetylated tubulin. Single clusters were counted in randomly selected areas of 5 μm^2. A total region of at least 280 μm^2 was evaluated for each protein in 3 individual animals. (**E**) Cluster diameter measured in stainings of ANO2, ANO6, and CNGA2. A total region of 500 μm^2 was evaluated for each protein in 3 individual animals.

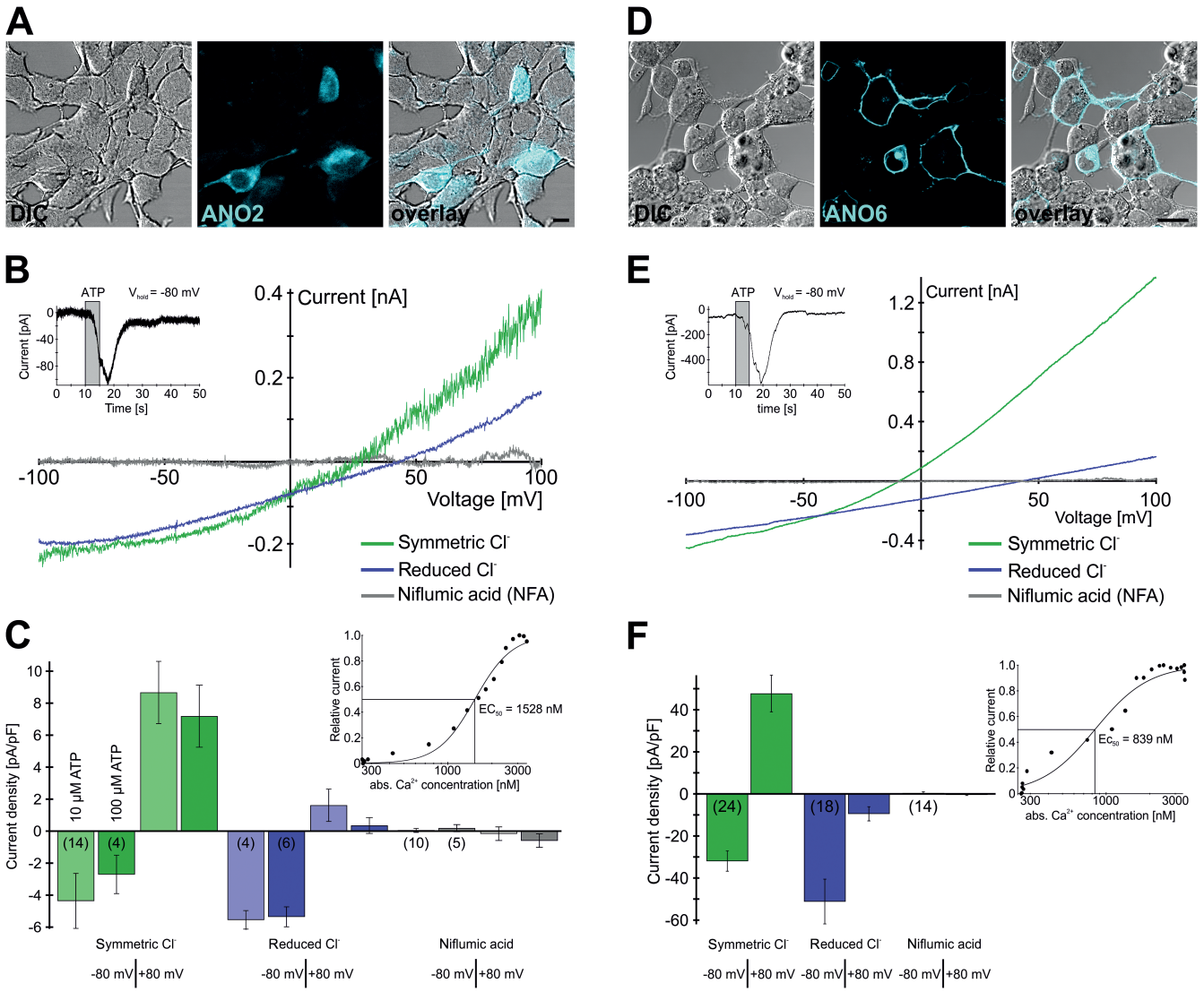

Figure 4 Recombinant ANO2 and ANO6 form Ca^{2+}-activated Cl^- channels. (**A**) ANO2-GFP[2] is expressed in the plasma membrane of HEK293T cells. (**B**) ATP stimulation activates chloride currents. In ramp protocols ranging from −100 to +100 mV, the reversal potential is shifted by reduction of extracellular chloride and currents are inhibited by niflumic acid. Inset: ATP application (5 s, gray bar) during continuous recording (V_{hold} = −80 mV) results in a negative current. (**C**) Maximal current densities at −80 and +80 mV (mean ± SEM). Two different ATP concentrations (10 and 100 µM) trigger similar current amplitudes under symmetric chloride (10 µM of ATP: n = 14; 100 µM of ATP: n = 4), reduced chloride (10 µM of ATP: n = 4; 100 µM of ATP: n = 6), and niflumic acid (10 µM of ATP: n = 10; 100 µM of ATP: n = 5) conditions. Inset: Dose–response relationship of chloride currents. The calculated EC_{50} for ANO2 is 1.53 µM of calcium. (**D**) ANO6-GFP[2] is expressed in the plasma membrane of HEK293T cells. (**E**) Stimulation with 100 µM of ATP activates chloride currents in patch-clamp experiments. In ramp protocols ranging from −100 to +100 mV, the reversal potential is shifted upon reduction of extracellular chloride and currents are inhibited by niflumic acid. Inset: ATP application (5 s, gray bar) during continuous recordings (V_{hold} = −80 mV) results in a negative current. (**F**) Maximal current densities at −80 and +80 mV (mean ± SEM) in presence of symmetric chloride (n = 24), reduced chloride (n = 18), and niflumic acid (n = 14). Inset: Dose–response relationship of chloride currents. The calculated EC_{50} for ANO6 is 839 nM of calcium. The current densities of ANO6 are significantly larger compared with ANO2 (Student's t-test, $P < 0.01$).

ATP), and −2.71 ± 1.2 pA/pF and 7.19 ± 1.9 pA/pF, respectively (n = 4; 100 µM of ATP). Under reduced extracellular chloride (solution S_3), current densities were −5.54 ± 0.6 pA/pF and 1.76 ± 1.6 pA/pF, respectively (n = 4; 10 µM of ATP), and −5.36 ± 0.6 pA/pF and 0.35 ± 0.5 pA/pF, respectively (n = 6; 100 µM of ATP). Treatment with niflumic acid (300 µM) strongly reduced currents: 0.04 ± 0.1 pA/pF and −0.16 ± 0.4 pA/pF, respectively (n = 10; 10 µM of ATP), and 0.19 ± 02 pA/pF and −0.59 ± 0.4 pA/pF, respectively (n = 5; 100 µM of ATP). As we did not observe significant differences in current amplitudes evoked by either 10 or 100 µM of ATP, subsequent experiments used 100 µM of ATP to mediate cytosolic Ca^{2+} elevations.

Next, we expressed recombinant ANO6-GFP[2]. Confocal microscopy of transfected cells revealed robust fluorescent membrane staining (Figure 4D). In whole-cell patch-clamp

recordings from fluorescently labeled cells, we observed Ca^{2+}-activated chloride currents (Figure 4E). As observed for ANO2-mediated currents, the reversal potential shifted when replacing external chloride with gluconate, and currents were blocked by niflumic acid (Figure 4E). Under symmetric chloride conditions, average current densities at −80 and +80 mV were −31.94 ± 4.8 and 47.73 ± 8.7 pA/pF, respectively (n = 24, Figure 4F). Reducing extracellular chloride resulted in current densities of −51.19 ± 10.6 and −9.47 ± 3.4 pA/pF (n = 18, Figure 4F). Niflumic acid blocked these currents (0.4 ± 0.6 and −0.3 ± 0.5 pA/pF [n = 14, Figure 4F]). For both ANO2 and ANO6, current properties remained essentially unaltered when voltage ramp directionality was inversed (+100 to −100 mV; data not shown). Together, our results thus indicate that ANO6 indeed acts as a Ca^{2+}-activated Cl^- channel.

Compared with ANO2, current amplitudes mediated by ANO6 were significantly larger (Student's t-test, $P < 0.01$). To analyze the dose–response relationship, we performed Ca^{2+}-imaging experiments in HEK293T cells and calculated the Ca^{2+} concentration after the ATP stimulation (Grynkiewicz et al. 1985). The currents measured for ANO2 and ANO6 were then plotted as a function of the Ca^{2+} concentration measured and fitted using the Hill equation. Hill coefficients were η = 3.4 for ANO2 and η = 2.3 for ANO6. For ANO2, the EC_{50} is approximately 1.5 µM (Figure 4C, inset), similar to the EC_{50} value of approximately 1.8 µM reported by Stephan et al. (2009). For ANO6, we calculated an EC_{50} of approximately 0.8 µM (Figure 4F, inset), indicating a slightly higher Ca^{2+} sensitivity of ANO6 compared with ANO2.

Recombinant ANO2 interacts with ANO6

Because ANO2 and ANO6 both form Ca^{2+}-activated Cl^- channels and are both localized in OSN cilia, we investigated whether both proteins form complexes in heterologous cells. Homodimerization of ANO2 and ANO6 has been described previously (Suzuki et al. 2010; Tien et al. 2013), but heteromerization has not been reported yet (Tien et al. 2013). To investigate the formation of homo- and heteromeric complexes, we performed BRET assays. N- and C-terminal fusion constructs of ANO2 and ANO6 with GFP^2 and *Renilla* luciferase were generated and expressed in HEK293T cells. Fluorescence microscopy confirmed expression and plasma membrane localization of all constructs (Figure 5A). In addition, luciferase fusion constructs were tested for luciferase activity (data not shown).

Next, we co-transfected GFP^2 and luciferase constructs and compared the resulting BRET ratios to control cells lacking GFP^2 as fluorescence acceptor. Significant BRET signals were observed upon co-expression of ANO2-*R*Luc and ANO2-GFP^2, and upon co-expression of ANO6-*R*Luc and ANO6-GFP^2 (Figure 5B). Ratios were 1.40 ± 0.05 compared with the control value of 1.1 ± 0.08 for ANO2 (n = 8), and 2.72 ± 0.35 compared with the control value of 0.97 ± 0.06 for ANO6 (n = 4), indicating homomerization of both channels. To exclude that measured signals just reflect molecular crowding of proteins, we raised the donor versus acceptor ratios and monitored BRET values (Figure 5C). The responses showed saturation when plotted against the relative amount of cDNA for the GFP^2 fusion construct, confirming that complex formation is specific. Thus, both anoctamin subtypes are capable of forming homomeric structures. We further noticed a persistent homomeric interaction of ANO2 and ANO6 by western blot analysis (Figure 5D. Although samples were subjected to rigorous denaturation treatment (10 min 95 °C, 4% [w/v] SDS, 100 mM of dithiothreitol), ANO2 and ANO6 displayed not only monomeric but also a presumably dimeric configuration.

We then investigated possible heteromerization of both anoctamin subtypes. Co-expression of ANO2 and ANO6 leads to strong overlap of the proteins at the plasma membrane (Figure 5E). The pair ANO2-*R*Luc and ANO6-GFP^2 showed a strong response and a nearly saturating BRET curve (Figure 5C), showing a specific interaction of ANO6 and ANO2 (ANO2 vs. ANO6 = 1.76 ± 0.07, control = 1.19 ± 0.04, n = 3).

Heteromerization of ANO2 and ANO6 results in supra-additive chloride currents

Because BRET assay results indicate interaction of recombinant ANO2 and ANO6, we used patch-clamp recordings and calcium imaging to unravel a possible functional role of this interaction. To identify cells transfected with both ANO2 and ANO6, constructs were labeled with different fluorescent tags (Figure 6A). In continuous recordings, we observed large negative currents upon stimulation with ATP (V_{hold} = −80 mV, Figure 6B inset). In ramp recordings, we confirmed that these signals correspond to Ca^{2+}-activated chloride currents (Figure 6B). Average current densities for putative ANO2/ANO6 multimers at −80 and +80 mV are shown in Figure 6C. Amplitudes were −82.86 ± 20.3 and 98.34 ± 20.3 pA/pF, respectively (n = 13; S_2), and −65.78 ± 17.7 and 0.76 ± 4.8 pA/pF, respectively (n = 11; S_3). These currents were also blocked by niflumic acid: −0.14 ± 0.5 pA/pF and −1.13 ± 0.8 pA/pF (n = 11). Thus, our results indicate that cotransfection of ANO2 and ANO6 results in supra-additive chloride currents, which are significantly larger (Student's t-test, $P < 0.05$) than the sum of ANO2 and ANO6 currents alone (Figure 6D). Currents mediated by both ANO2 and ANO6 homomers as well as by putative ANO2/ANO6 multimers all reversed at approximately 0 mV under conditions of equimolar Cl^- concentrations (S_2; Figure 6D, inset). The calculated EC_{50} for Ca^{2+} activation of putative ANO2/ANO6 multimers is similar to the EC_{50} value calculated for ANO6 (793 and 839 nM, respectively; Figure 6C, inset; η = 1.9).

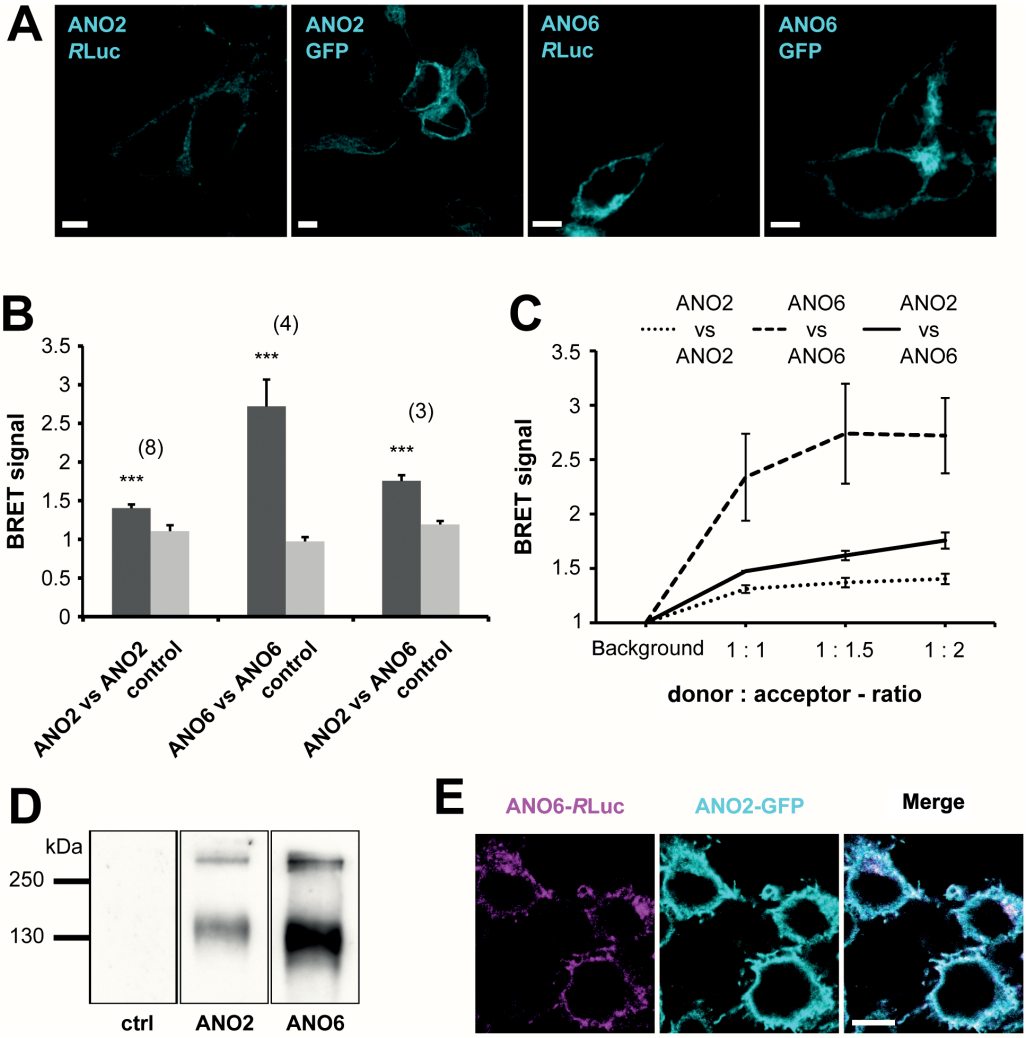

Figure 5 ANO2 and ANO6 form homomers and heteromers. (**A**) Surface expression of anoctamins in HEK293T cells used in BRET assays. ANO2-GFP, ANO2-*R*Luc, ANO6-GFP, and ANO6-*R*Luc were labeled by specific antibodies against GFP and Luciferase. Scale bars = 5 µm. (**B**) BRET signals from cells expressing ANO2 and ANO6 in homomeric and heteromeric combinations. Shown are normalized BRET signals of *R*Luc and GFP fusion proteins in a ratio of 1:2. Controls are cells transfected with *R*Luc-tagged protein together with the respective non-tagged protein in a ratio of 1:2. (**C**) BRET signals as a function of increased acceptor (GFP-tagged construct) concentrations for different anoctamin combinations; error bars represent SEM. (**D**) Equal amounts of GFP-tagged ANO2 and ANO6, expressed in HEK293T cells, were loaded onto SDS–polyacrylamide gel electrophoresis and subjected to western blotting. Despite harsh denaturation treatment (10 min 95 °C, 4% [w/v] SDS), blots not only showed monomeric proteins but also putative dimers approximately double the size of the monomer. (**E**) Co-expression of ANO6-*R*Luc and ANO2-GFP in HEK293T cells, analyzed by antibody staining for *R*Luc and GFP, showing that most of the recombinant protein is localized at the plasma membrane.

Co-localization of ANO2 and ANO6 in ciliary microdomains

Next, we asked whether ANO2 and ANO6 may co-localize in olfactory cilia. STED microscopy of preparations where both channels were labeled revealed a pattern of closely associated spot-like structures, which did not completely overlap (Figure 7A). We compared this staining pattern to co-labeled CNGA2 and CNGA4, another CNG channel subunit (Figure 7B). Native olfactory CNG channels are heterotetramers, consisting of 2 CNGA2, 1 CNGA4 and 1 CNGB1b subunits (Zheng and Zagotta 2004). As expected, CNGA4 staining revealed a distribution pattern similar to CNGA2. Co-labeling of both subunits showed closely associated spot-like structures that do not completely overlap, very similar to the localization of ANO2 and ANO6 (Figure 7A). The similar staining patterns for CNGA2/CNGA4 and ANO2/ANO6, respectively, therefore support the notion that ANO2 and ANO6 form oligomeric complexes in olfactory cilia. Moreover, western blot analysis of olfactory tissue revealed that both ANO2 and ANO6 antibodies detected a band at the expected size of a dimeric protein (Figure 7C). Both proteins have virtually the same molecular weight, potential homo-and hetero-oligomers can therefore not be distinguished by size.

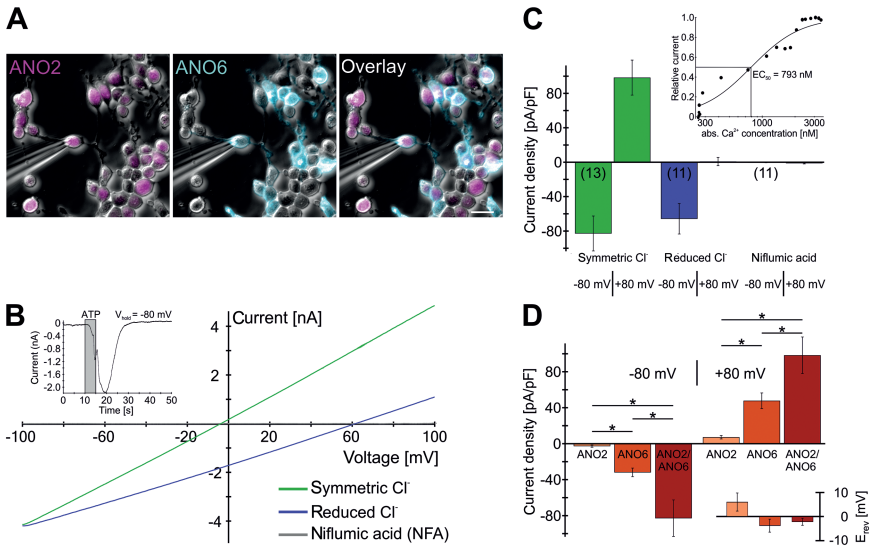

Figure 6 ANO2 and ANO6 co-expression results in supra-additive currents. (**A**) Cells expressing ANO2 and ANO6 identified *via* different fluorescent tags (ANO2-TC, ANO6-GFP[2]). (**B**) ATP stimulation (100 μM) activates chloride currents in patch-clamp experiments. In ramp protocols ranging from −100 to +100 mV, the reversal potential is shifted if extracellular chloride is reduced. Currents are inhibited by niflumic acid. Inset: ATP application (5 s, gray bar) during continuous recording (V_{hold} = −80 mV) results in large negative currents. (**C**) Maximal current densities at −80 and +80 mV (mean ± SEM) under symmetric chloride (n = 13), reduced chloride (n = 11), and niflumic acid (n = 11) conditions. Inset: Dose–response relationship of chloride currents. The calculated EC_{50} for putative ANO2/ANO6 multimers is 793 nM of calcium. (**D**) Comparison of the current densities at −80 and +80 mV recorded in cells (co) expressing recombinant ANO2, ANO6, and ANO2/ANO6. The currents of ANO2/ANO6 expressing cells are significantly larger compared with the currents of ANO2 or ANO6 alone (Student's t-test, $P < 0.05$). Inset shows the average reversal potential of ANO2-, ANO6-, and ANO2-/ANO6-dependent currents derived from ramp recordings under symmetric chloride conditions (6.0 ± 3.8 mV, n = 4 [ANO2]; −3.8 ± 2.7 mV, n = 24 [ANO6]; −2.2 ± 1.5 mV, n = 13 [ANO2/ANO6]; mean ± SEM).

Discussion

We report here that besides ANO2 another anoctamin family member, ANO6, is also localized to OSN cilia. Similar to ANO2, ANO6 forms a Ca^{2+}-activated Cl^- channel and could therefore be involved in signal transduction. STED microscopy reveals that ANO2, ANO6, and the CNG channel subunits CNGA2 and CNGA4 are localized in morphologically similar ciliary microdomains. Biochemical, imaging, and physiological approaches demonstrate that recombinant ANO6, at least to some extent, oligomerizes with ANO2. Oligomerization alters channel properties in heterologous cells and, possibly, also in OSNs.

Olfactory signaling proteins are organized in microdomains

The topology of CNGA2, ANO2, and ANO6 ion channels provides evidence for a compartmentalized and confined distribution in the ciliary membrane, indicating the formation of signaling microdomains. Such spatially restricted microdomains have also been proposed after detailed analysis of odorant responses with electrophysiological (Bhandawat et al. 2010) and Ca^{2+} imaging methods (Castillo et al. 2010), but their detailed localization remained unclear. Recent super-resolution imaging of immunostained ACIII in primary cilia of human fibroblasts also showed that instead of a homogeneous distribution along the primary cilium, ACIII forms a periodic punctuate pattern (Yang et al. 2013). Our results demonstrate the potential of 2-color STED super-resolution microscopy to reveal novel structural characteristics in sensory cilia. Previous work estimated that Ca^{2+}-activated Cl^- channel density in olfactory cilia was 62 μm^{-2}, whereas CNG channel density was 8 μm^{-2} (Reisert et al. 2003). The density of the patches observed here was approximately 3 μm^{-2} for CNGA2 and 5 μm^{-2} for ANO2. Although the absolute numbers differ to some extent, analysis of protein localization with STED microscopy in principle confirmed the finding that chloride channel density is higher than the density of CNG channels. Differences in absolute numbers likely result from different experimental approaches because we cannot determine whether patches contain 1 or more channel proteins.

The spatial distribution of signaling proteins in the olfactory system is controversial. In most studies, the distribution along the cilia has been investigated primarily. Cyclic nucleotide sensitivity has been found along the entire cilium in salamander (Lowe and Gold 1991). CNGA2 was localized predominantly to the tip of rat cilia with electron microscopy (Matsuzaki et al. 1999). Inside-out ciliary preparations together with a cAMP diffusion model are suggestive of CNG channel clustering in the mid-section of frog olfactory cilia (Flannery et al. 2006). In cryosections, the density of intermingled cilia on the olfactory epithelial surface precludes continuous analysis of single cilia, but CNG channels

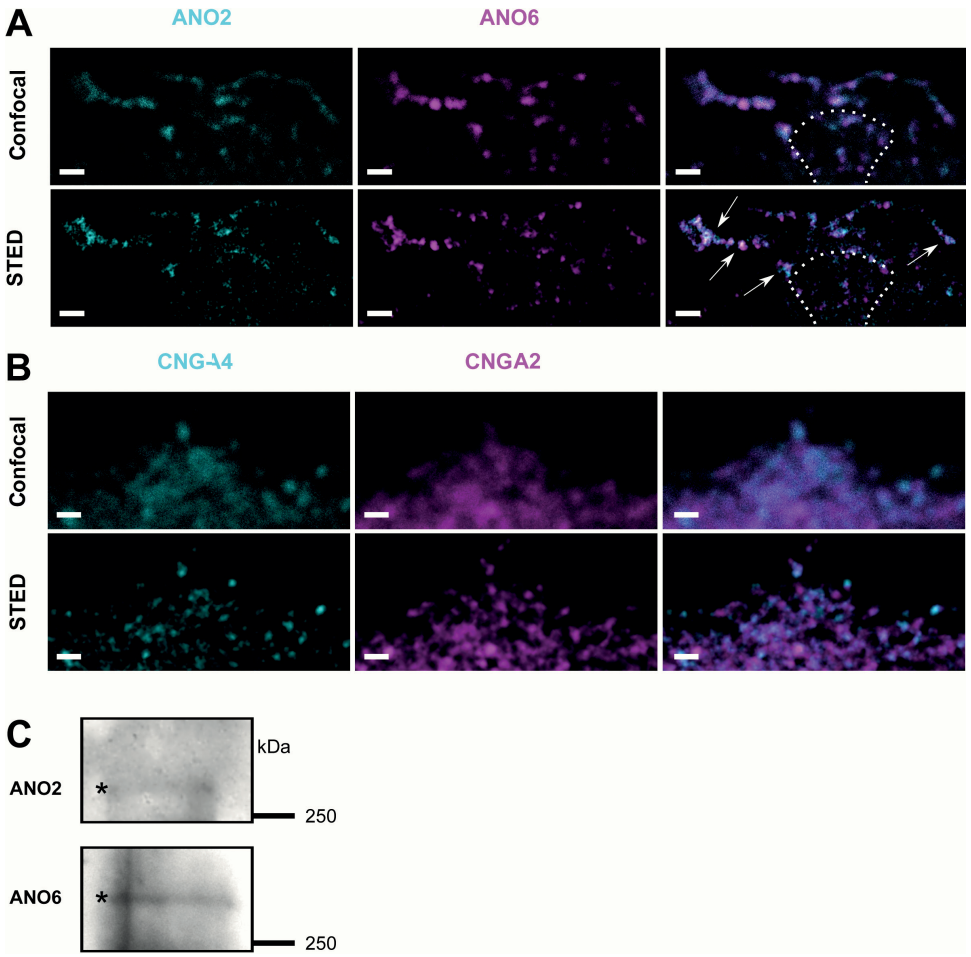

Figure 7 Co-localization of ANO2 and ANO6 in olfactory cilia. (**A**) High-magnification confocal and STED images of olfactory cilia stained for ANO2 (cyan) and ANO6 (magenta). Position of the dendritic knob is marked by a punctate line. Arrows point to spots showing closed apposition of spots. (**B**) High-magnification confocal and STED images of olfactory cilia stained for CNGA4 (cyan) and CNGA2 (magenta). Scale bars = 1 μm (anoctamins); 500 nm (CNG channel). (**C**) Western blot of membrane fractions from olfactory epithelium membrane show ANO2 and ANO6 proteins in potentially dimeric form.

and ANOs seem to be evenly distributed in the ciliary layer. Local uncaging of cytoplasmic-caged compounds with nano-scale UV-laser stimulation showed that newt olfactory neurons respond to stimuli at any point of the cilia (Takeuchi and Kurahashi 2008), showing that olfactory transduction channels are broadly distributed along the cilia. An even distribution of signals elicited by a laser beam with a diameter in the micrometer range as described by Takeuchi and Kurahashi is consistent with a clustered distribution of 3–5 patches/μm^2 revealed by STED analysis.

ANO6 could be part of the ciliary signal transduction cascade

Domain diameters assessed by 3 different antibodies were similar. Given the similarities in CNGA2, ANO2, and ANO6 distribution, this finding indicates that ANO6 could also be part of the olfactory signal transduction cascade. It is unclear whether all members of the anoctamin family form Ca^{2+}-activated Cl^- channels and reports on ANO6 function as a plasma membrane Ca^{2+}-activated Cl^- channel are inconsistent (Schreiber et al. 2010; Suzuki et al. 2010; Tian et al. 2012). We show here that ANO6, similar to ANO2, is localized at the membranes of both heterologous cells and at olfactory cilia. Moreover, our electrophysiological data confirm other studies that describe ANO6 as Ca^{2+}-activated Cl^- channel (Kmit et al. 2013; Martins et al. 2011), adding another potentially contributing component to the elusive olfactory Ca^{2+}-activated Cl^- channel.

Physiological relevance of anoctamin oligomerization

Several studies show a homodimerization of ANO1 (Fallah et al. 2011; Sheridan et al. 2011; Tien et al. 2013). In general, members of the anoctamin family share a putative homodimeric architecture facilitated by their cytoplasmic N-termini, which is important for channel assembly. Amino acid substitutions in the dimerization domain affect functional expression of ANO1, indicating a critical role of channel dimerization in subunit assembly (Tien et al. 2013). Using

BRET assays, we show that ANO2 and ANO6 are capable of forming homo-oligomers in HEK293T cells. This is consistent with a recent study showing coimmunoprecipitation of both proteins (Tien et al. 2013). We not only found homomeric interaction of ANO2 and ANO6, respectively, but also identified heteromeric interactions between ANO2 and ANO6. These heteromeric interaction has not been found by immunoprecipitation (Tien et al. 2013), which could reflect the differences between both types of assays. Because we found both proteins in the OSN cilia and because they localize to the same microdomains, we assume that interaction could also occur in olfactory cilia. This hetero-oligomerization likely has physiological relevance because co-expression of both recombinant channels leads to markedly increased chloride current densities. Another parameter that differs in cells expressing recombinant ANO2 alone versus cells co-expressing ANO2 and ANO6 is the channels' apparent Ca^{2+} sensitivity.

In summary, we show here that ANO6 is localized to microdomains in olfactory cilia. Hetero-oligomerization with ANO2 influences the physiological properties of ANO2, indicating that ANO6 plays a role in olfactory signal transduction. Our results indicate that the native Ca^{2+}-activated Cl^- channels in olfactory neurons may be heteromers composed of several anoctamin subtypes.

Supplementary material

Supplementary material can be found at http://www.chemse.oxfordjournals.org/

Funding

This work was supported by the Deutsche Forschungsgemeinschaft [SPP1392, Exc257, and SFB958] and the Volkswagen Foundation.

Acknowledgements

M.S. is a Lichtenberg Professor of the Volkswagen Foundation. We thank K. Kunzelmann and R. Schreiber (University of Regensburg, Germany) for donation of the anti-ANO6 antibody as well as the antigenic peptide, and M. Biel (LMU Munich, Germany) for donation of the anti-CNGA4 antibody. ANO2-eGFP was kindly provided by H. Zhao (Johns Hopkins University, Baltimore).

References

Baumgart S, Jansen F, Bintig W, Kalbe B, Herrmann C, Klumpers F, Köster SD, Scholz P, Rasche S, Dooley R, *et al*. 2014. The scaffold protein MUPP1 regulates odorant-mediated signaling in olfactory sensory neurons. J Cell Sci. 127:2518–2527.

Belluscio L, Gold GH, Nemes A, Axel R. 1998. Mice deficient in G(olf) are anosmic. Neuron. 20(1):69–81.

Bhandawat V, Reisert J, Yau KW. 2005. Elementary response of olfactory receptor neurons to odorants. Science. 308(5730):1931–1934.

Bhandawat V, Reisert J, Yau KW. 2010. Signaling by olfactory receptor neurons near threshold. Proc Natl Acad Sci USA. 107(43):18682–18687.

Billig GM, Pál B, Fidzinski P, Jentsch TJ. 2011. Ca2+-activated Cl– currents are dispensable for olfaction. Nat Neurosci. 14(6):763–769.

Boccaccio A, Menini A. 2007. Temporal development of cyclic nucleotide-gated and Ca2+ -activated Cl- currents in isolated mouse olfactory sensory neurons. J Neurophysiol. 98(1):153–160.

Buck L, Axel R. 1991. A novel multigene family may encode odorant receptors: a molecular basis for odor recognition. Cell. 65(1):175–187.

Caputo A, Caci E, Ferrera L, Pedemonte N, Barsanti C, Sondo E, Pfeffer U, Ravazzolo R, Zegarra-Moran O, Galietta LJ. 2008. TMEM16A, a membrane protein associated with calcium-dependent chloride channel activity. Science. 322(5901):590–594.

Castillo K, Restrepo D, Bacigalupo J. 2010. Cellular and molecular Ca2+ microdomains in olfactory cilia support low signaling amplification of odor transduction. Eur J Neurosci. 32(6):932–938.

Dauner K, Lissmann J, Jeridi S, Frings S, Möhrlen F. 2012. Expression patterns of anoctamin 1 and anoctamin 2 chloride channels in the mammalian nose. Cell Tissue Res. 347(2):327–341.

Dooley R, Baumgart S, Rasche S, Hatt H, Neuhaus EM. 2009. Olfactory receptor signaling is regulated by the post-synaptic density 95, Drosophila discs large, zona-occludens 1 (PDZ) scaffold multi-PDZ domain protein 1. FEBS J. 276(24):7279–7290.

Dyba M, Jakobs S, Hell SW. 2003. Immunofluorescence stimulated emission depletion microscopy. Nat Biotechnol. 21(11):1303–1304.

Fallah G, Römer T, Detro-Dassen S, Braam U, Markwardt F, Schmalzing G. 2011. TMEM16A(a)/anoctamin-1 shares a homodimeric architecture with CLC chloride channels. Mol Cell Proteomics. 10(2):M110.004697.

Flannery RJ, French DA, Kleene SJ. 2006. Clustering of cyclic-nucleotide-gated channels in olfactory cilia. Biophys J. 91(1):179–188.

Giepmans BN, Adams SR, Ellisman MH, Tsien RY. 2006. The fluorescent toolbox for assessing protein location and function. Science. 312(5771):217–224.

Grynkiewicz G, Poenie M, Tsien RY. 1985. A new generation of Ca2+ indicators with greatly improved fluorescence properties. J Biol Chem. 260(6):3440–3450.

Hengl T, Kaneko H, Dauner K, Vocke K, Frings S, Möhrlen F. 2010. Molecular components of signal amplification in olfactory sensory cilia. Proc Natl Acad Sci USA. 107(13):6052–6057.

Kato A, Touhara K. 2009. Mammalian olfactory receptors: pharmacology, G protein coupling and desensitization. Cell Mol Life Sci. 66(23):3743–3753.

Kleene SJ, Gesteland RC. 1991. Calcium-activated chloride conductance in frog olfactory cilia. J Neurosci. 11(11):3624–3629.

Kmit A, van Kruchten R, Ousingsawat J, Mattheij NJ, Senden-Gijsbers B, Heemskerk JW, Schreiber R, Bevers EM, Kunzelmann K. 2013. Calcium-activated and apoptotic phospholipid scrambling induced by Ano6 can occur independently of Ano6 ion currents. Cell Death Dis. 4:e611.

Kunzelmann K, Nilius B, Owsianik G, Schreiber R, Ousingsawat J, Sirianant L, Wanitchakool P, Bevers EM, Heemskerk JW. 2014. Molecular functions of anoctamin 6 (TMEM16F): a chloride channel, cation channel, or phospholipid scramblase? Pflugers Archiv: Eur J Physiol. 466:407–414.

Kurahashi T, Yau KW. 1993. Co-existence of cationic and chloride components in odorant-induced current of vertebrate olfactory receptor cells. Nature. 363(6424):71–74.

Lowe G, Gold GH. 1991. The spatial distributions of odorant sensitivity and odorant-induced currents in salamander olfactory receptor cells. J Physiol. 442:147–168.

Lowe G, Gold GH. 1993. Nonlinear amplification by calcium-dependent chloride channels in olfactory receptor cells. Nature. 366(6452):283–286.

Martins JR, Faria D, Kongsuphol P, Reisch B, Schreiber R, Kunzelmann K. 2011. Anoctamin 6 is an essential component of the outwardly rectifying chloride channel. Proc Natl Acad Sci USA. 108(44): 18168–18172.

Matsuzaki O, Bakin RE, Cai X, Menco BP, Ronnett GV. 1999. Localization of the olfactory cyclic nucleotide-gated channel subunit 1 in normal, embryonic and regenerating olfactory epithelium. Neuroscience. 94(1): 131–140.

Michalakis S, Reisert J, Geiger H, Wetzel C, Zong X, Bradley J, Spehr M, Hüttl S, Gerstner A, Pfeifer A, *et al*. 2006. Loss of CNGB1 protein leads to olfactory dysfunction and subciliary cyclic nucleotide-gated channel trapping. J Biol Chem. 281(46):35156–35166.

Munger SD, Leinders-Zufall T, Zufall F. 2009. Subsystem organization of the mammalian sense of smell. Annu Rev Physiol. 71:115–140.

Nakamura T, Gold GH. 1987. A cyclic nucleotide-gated conductance in olfactory receptor cilia. Nature. 325(6103):442–444.

Pifferi S, Boccaccio A, Menini A. 2006. Cyclic nucleotide-gated ion channels in sensory transduction. FEBS Lett. 580(12):2853–2859.

Pifferi S, Dibattista M, Menini A. 2009. TMEM16B induces chloride currents activated by calcium in mammalian cells. Pflugers Arch. 458(6):1023–1038.

Pifferi S, Menini A, Kurahashi T. 2010. Signal transduction in vertebrate olfactory cilia. In: Menini A, editor. The neurobiology of olfaction. Boca Raton (FL): http://www.crcpress.com/; CRC Press. p. 203-224. ISBN-13: 978-1-4200-7197-9.

Rasche S, Toetter B, Adler J, Tschapek A, Doerner JF, Kurtenbach S, Hatt H, Meyer H, Warscheid B, Neuhaus EM. 2010. Tmem16b is specifically expressed in the cilia of olfactory sensory neurons. Chem Senses. 35(3):239–245.

Reisert J, Bauer PJ, Yau KW, Frings S. 2003. The Ca-activated Cl channel and its control in rat olfactory receptor neurons. J Gen Physiol. 122(3):349–363.

Reisert J, Lai J, Yau KW, Bradley J. 2005. Mechanism of the excitatory Cl- response in mouse olfactory receptor neurons. Neuron. 45(4):553–561.

Sagheddu C, Boccaccio A, Dibattista M, Montani G, Tirindelli R, Menini A. 2010. Calcium concentration jumps reveal dynamic ion selectivity of calcium-activated chloride currents in mouse olfactory sensory neurons and TMEM16b-transfected HEK 293T cells. J Physiol. 588: 4189–4204.

Schmidt R, Wurm CA, Jakobs S, Engelhardt J, Egner A, Hell SW. 2008. Spherical nanosized focal spot unravels the interior of cells. Nat Methods. 5(6):539–544.

Schreiber R, Uliyakina I, Kongsuphol P, Warth R, Mirza M, Martins JR, Kunzelmann K. 2010. Expression and function of epithelial anoctamins. J Biol Chem. 285(10):7838–7845.

Schroeder BC, Cheng T, Jan YN, Jan LY. 2008. Expression cloning of TMEM16A as a calcium-activated chloride channel subunit. Cell. 134(6):1019–1029.

Sheridan JT, Worthington EN, Yu K, Gabriel SE, Hartzell HC, Tarran R. 2011. Characterization of the oligomeric structure of the Ca(2+)-activated Cl- channel Ano1/TMEM16A. J Biol Chem. 286(2):1381–1388.

Stephan AB, Shum EY, Hirsh S, Cygnar KD, Reisert J, Zhao H. 2009. ANO2 is the cilial calcium-activated chloride channel that may mediate olfactory amplification. Proc Natl Acad Sci USA. 106(28):11776–11781.

Suzuki J, Umeda M, Sims PJ, Nagata S. 2010. Calcium-dependent phospholipid scrambling by TMEM16F. Nature. 468(7325):834–838.

Takeuchi H, Kurahashi T. 2008. Distribution, amplification, and summation of cyclic nucleotide sensitivities within single olfactory sensory cilia. J Neurosci. 28(3):766–775.

Tian Y, Schreiber R, Kunzelmann K. 2012. Anoctamins are a family of Ca2+-activated Cl- channels. J Cell Sci. 125:4991–4998.

Tien J, Lee HY, Minor DL Jr, Jan YN, Jan LY. 2013. Identification of a dimerization domain in the TMEM16A calcium-activated chloride channel (CaCC). Proc Natl Acad Sci USA. 110(16):6352–6357.

Veitinger S, Veitinger T, Cainarca S, Fluegge D, Engelhardt CH, Lohmer S, Hatt H, Corrazza S, Spehr J, Neuhaus EM, *et al*. 2011a. Mitochondrial Ca2+ mobilization in purinergic mouse sertoli cell signaling. J Physiol. 589:5033–5055.

Veitinger T, Riffell JR, Veitinger S, Nascimento JM, Armon L, Triller A, Chandsawangbhuwana C, Schwane K, Geerts A, Wunder F, *et al*. 2011b. Chemosensory Ca2+ dynamics correlate with diverse behavioral phenotypes in human sperm. J Biol Chem. 286:17311–17325.

Wong ST, Trinh K, Hacker B, Chan GC, Lowe G, Gaggar A, Xia Z, Gold GH, Storm DR. 2000. Disruption of the type III adenylyl cyclase gene leads to peripheral and behavioral anosmia in transgenic mice. Neuron. 27(3):487–497.

Yang TT, Hampilos PJ, Nathwani B, Miller CH, Sutaria ND, Liao JC. 2013. Superresolution STED microscopy reveals differential localization in primary cilia. Cytoskeleton (Hoboken). 70(1):54–65.

Yang YD, Cho H, Koo JY, Tak MH, Cho Y, Shim WS, Park SP, Lee J, Lee B, Kim BM, *et al*. 2008. TMEM16A confers receptor-activated calcium-dependent chloride conductance. Nature. 455(7217):1210–1215.

Zheng J, Zagotta WN. 2004. Stoichiometry and assembly of olfactory cyclic nucleotide-gated channels. Neuron. 42(3):411–421.